2
Literature Review

2.1 PHOTOVOLTAIC ENERGY CONVERSION – A BRIEF HISTORY

Long before the concept of solar energy was realized, man used mirrors and concentrating gasses like magnifying glasses to light fire and burn. During 3rd and 2nd century BC, Greeks and Romans used mirrors to light for religious purposes and by Chinese during 20th century AD. In 1767, Horace de Saussure built the first solar collector which was later used as solar cooker by Sir John Herschel. Edmund Becquerel discovered the photovoltaic effect in 1839 and observed that electricity generation in an electricity conducting solution is increased when exposed to sunlight [Becquerel, 1839]. During 1860s August Mouchet developed an idea for solar powered steam engine which laid the foundation for the modern day parabolic dish collectors. In 1873 Willoughby Smith discovered the photoconductive property of Selenium [Smith, 1873] and in 1876 William Grylls Adams and Richard Evans Day discovered that it can produce electricity on exposure to light and proved that solid materials could be used to change light into electricity and Charles Fritts described the first solar cells made of Selenium wafers in 1883 [Fritts, 1883]. In 1880 Samuel P Langley invented the device bolometer that can be used to measure light from sun rays. Ultraviolet rays were used to cause spark to jump between two electrodes by Heinrich Hertz in 1883, this leads to invention of the first solar water heater by Clarence Kemp. Early 1900s was marked by series of inventions, in 1904 Wilhelm Hallwachs discovered photosensitivity in copper and cuprous oxide. A year later Einstein discovered the photoelectric effect. In 1908 William Bailley presented a rough design of solar collector with copper coils in an insulating box. In 1932 Audobert and Stora discovered the photovoltaic effect in Cadmium sulfide. The first theoretical calculation of the efficiency of different materials having varied band gap was done by Dr. Dan Trivich. In 1954 Daryl Chapin, Calvin Fuller and Gerald Pearson from Bell Labs developed the silicon photovoltaic cell capable of converting solar energy to electrical power [Chapin, 1954]. Designed in mid 1950s Bridgers-Paxton building is the first world's solar heated office. In 1956 GaAs pn junction based solar cells were reported by RCA Lab with 6% efficiency [Jenny, *et al.*, 1956]. The same year marked developing of photovoltaic cells for orbiting Earth satellites was proposed and in 1958 space cells resistant to radiation were fabricated by U.S. Signal Corps Laboratories in n-on-p silicon photovoltaic cells and Hoffman Electronics fabricated 9% efficient photovoltaic cells. In 1959 Explorer VI and VII were launched with photovoltaic arrays. A 242 watt, the then largest photovoltaic array was installed in a lighthouse in Japan in 1963 also SHARP corporation produced Si photovoltaic. The years after that was followed by various development including NASA's Nimbus program and launching of the 1 kilowatt photovoltaic powered Orbiting Astronomical Observatory. Years later in 1976 David Carlson and Christopher Wronski fabricated the first amorphous Si photovoltaic cells. In 1977 NREL (National Renewable Energy Lab) was launched by the Department of Energy in U.S., a facility dedicated solely to harnessing solar power.

University of Delaware successfully fabricated copper sulfide/cadmium sulfide based solar cells exceeding 10% efficiency in 1980. Solar Challenger – a solar powered aircraft was flown across the English Channel with over 16,000 solar cells producing 3 kilowatt power. Other companies like Volkswagen started mounting photovoltaic arrays on roofs of station wagons. By the year 1982 the worldwide solar production exceeded 9.3 megawatts and a year

later 21.3 megawatts. 20% efficiency barrier was broken for Si solar cell by University of south Wales in the year 1985 under 1 sun [Green, *et al.*, 1985]. Also, the world's largest solar thermal facility in California was commissioned with rows of mirrors to gather sun's energy onto pipes circulating heat transfer fluid which was used to produce steam to generate electricity. During the early 1990s there were great developments like the starting of DSSC (Dye sensitized solar cells) [O'Regan and Gratzel, 1991] and reaching 15.9% efficiency of cadmium telluride based thin film solar cells. Later on, NREL developed solar cell exceeding 30% efficiency based on gallium indium phosphide and gallium arsenide [Friedman, *et al.*, 1995]. Icare, developed at the University of Stuttgart was the then most advanced solar-powered plane and flew over Germany with 3000 solar cells covering 21 m² in 1996. The same year operation of Solar Two began, which marked a start for clean energy for future by means of efficient production and storage of solar power. Subhendu Guha led the foundation of flexible solar shingles which eventually led to Building Integrated Photovoltaics (BIPV). By the year 1999 worldwide installed photovoltaic capacity reached 1000 megawatts. 2000 and the years after that are marked by the incorporation of solar photovoltaics on a larger scale for domestic and residential use.

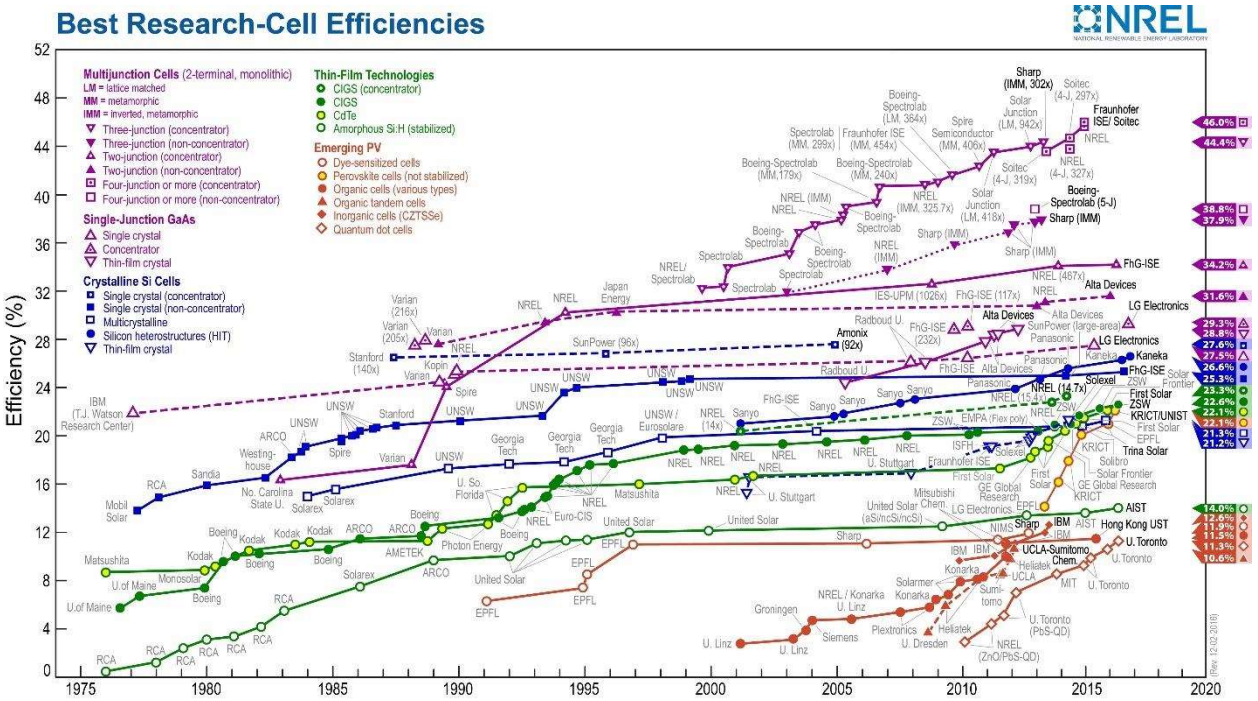

Figure 2.1 : Plot of compiled values of highest confirmed photo conversion efficiencies for research cells for various photovoltaic technologies from 1976 to the present. This plot is courtesy of the National Renewable Energy Laboratory, Golden, CO.

The up-to-date efficiencies of the devices included in the NREL plot have been confirmed by various independent, recognized test labs (e.g., NREL, AIST, Fraunhofer) and are reported on a standardized basis (see Figure 2.1).

The reference for the photovoltaic devices are done with reference to standards listed in IEC 60904-3 edition or ASTM G173. The measurements are performed according to standard test or reporting conditions (STC) according to which the reference temperature is 25°C and area is defined by total cell area. The cells reported here includes various generations of the solar cell with different families of semiconductors: (1) multi-junction cells, (2) single-junction gallium arsenide solar cells, (3) crystalline silicon solar cells, (4) thin film technologies, and (5) other emerging photovoltaics are indicated by different colours with the latest and the recent world record for all the technologies being highlighted on the right in a flag containing the recorded efficiency and the symbol of the technology. The plot also includes the organization and the institute fabricating the device.

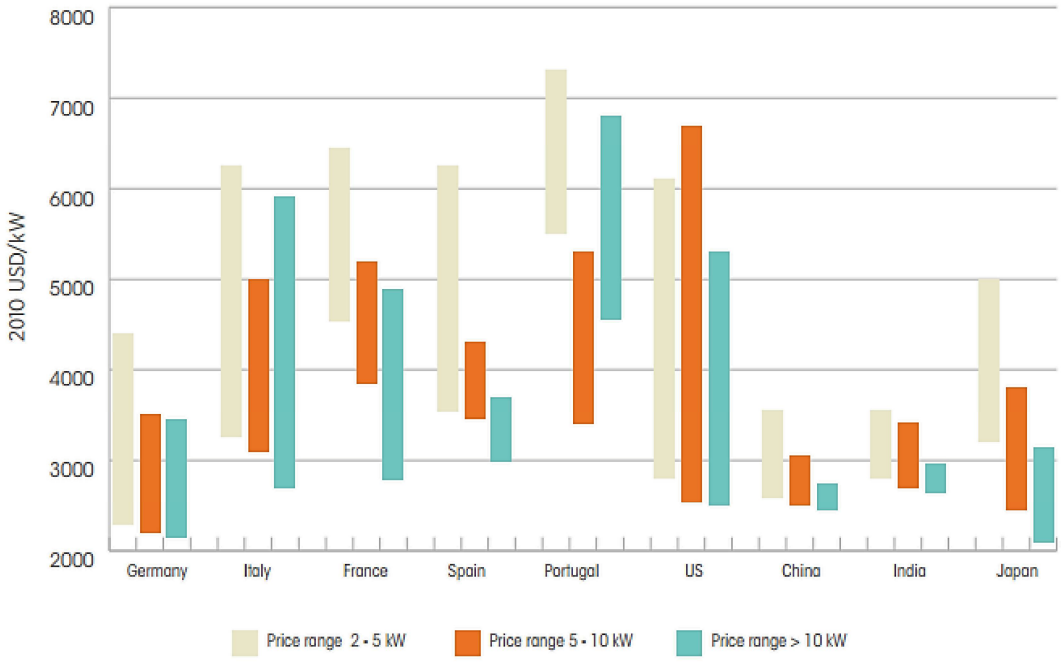

Figure 2.2 : Price range for residential applications in different countries for installed PV systems. (Source: Irena)

With its low costs and commercial efficiency, the 1st generation solar cells still dominate the market and are regarded as a mature PV technology along with well-established manufacturers (see Figure 2.2 and Table 2.1). The cost of production and the raw materials are relatively high despite its significant reduction over the past few years. Meanwhile, the 2nd generation thin film PV technology are increasingly becoming attractive because of its low cost in materials and manufacturing process but it is pulled down by the lower efficiency than the 1st generation. These generations are in early stage, have smaller market and optimization is still required in regards to durability, raw materials and toxicity. The 3rd generations are still on the verge of commercialization. Other upcoming PV technologies like DSSCs and Organic PV technology offers low efficiency but at a lower material cost and free-form shaping and could be one of future technology especially in solar driven solar powered electronic devices [IRENA, 2012].

Table 2.1: An overall comparison at Standard Temperature Conditions (STC) – 25° C temperature, light intensity 1000W/m^2, air mass 1.5, of some major PV technologies

	1st Generation PV		*2nd Generation PV*			*3rd Generation PV*		
Technology	*Single crystalline silicon (sc-Si)*	*Polycrystalline silicon (pc-Si)*	*Amorphous silicon (a-Si)*	*Copper Indium Gallium Diselenide (CIS/CIGS)*	*Copper Telluride Solar cells (CdTe)*	*III-V compudn Multijunction, Concentrated PV (CPV)*	*DSSC*	*Organic or Polymer (OPV)*
Best solar cell efficiency at AM 1.5*	24.7		10.4 Single Junction 13.2 Tandem	20.3	16.5	43.5	11.1	11.1

Confirmed Solar cell efficiency at AM 1.5	20-24	14-18	6-8	10-12	8-10	36-41	8.8	8.3
Confirmed PV module efficiency at AM 1.5	15-19	13-15	5-8	7-11	8-11	25-30	1-5	1
Confirmed maximum PV module efficiency	23	16	7.1/10.0	12.1	11.2	25	-	-
Cost PV module (USD/W)	< 1.4	< 1.4	~ 0.8	~ 0.9	~ 0.9	-	-	-
Market share in 2009	83	3	1	13	-	-	-	-
Market share in 2010	87	2	2	9	-	-	-	-
Maximum PV module output power (W)	320	-	300	120	120	120	-	
PV module size (m^2)	2	1.4-2.5	1.4	0.6-1.0	0.72	-	-	-

In 2008, NREL Labs in U.S. department of energy were able to achieve a record breaking 40% photon conversion efficiency of light to electricity. During the same year because of the global economic crisis, the Spanish government reduced subsidies rates given on the solar production which affected highly overall across other countries. By 2010, due to lack of market two leading solar based companies namely, Evergreen Solar and Solyndra failed. But the setback was soon recovered with China building Golmund Solar Park having installed capacity of 200 megawatts, the largest in the history of solar energy plant. This record was soon broken by India by building Gujarat Solar Park with installed capacity of 605 megawatts where the solar farms are dispersed all over various regions in the state of Gujarat.

2.2 DYE SENSITIZED SOLAR CELLS (DSSC)

DSSCs are photo-electrochemical cells that replaces the classical solid-state junction's contacting phase of the semiconductor with an electrolyte, liquid, solid or gel, developed by O'Regan and Graetzel in 1991 [O'Regan and Gratzel, 1991]. This device absorbs optically followed by a charge separation process by means of a sensitizer absorbed over a wide band gap nanocrystalline semiconductor. DSSCs offers low cost investment and fabrication unlike its other counterparts and apart from that it performs relatively better under diffuse light conditions and higher temperature as well. Moreover, DSSCs has the ease of flexibility in design – shape, color and transparency which opens up the viability of integration into a variety of products for commercial usage.

2.2.1 Basic structure and principles of DSSCs

The DSSC is a sandwich model at the heart of which is the wide band gap semiconductor coated over a transparent conducting oxide film (FTO/ITO) as shown in Figure 2.3a. The semiconductor most widely used is the TiO_2 with other alternatives like ZnO [Tennakone, *et al.*, 1999] and Nb_2O_5 [Sayama, *et al.*, 1998] are sensitized with a dye sensitizer and are in contact with a redox electrolyte or organic hole conductor. The sensitizer attached to the wide band semiconductor is absorbed as a monolayer that does the charge transfer when light falls and it gets excited transferring the electron to the oxide layer, the charge lost is restored when electron from the redox is donated to it. The electrolyte is an organic solvent capable of going redox, the most commonly used being the iodide/triiodide couple. The iodide is regenerated by the reduction of triiodide from the counter electrode which is completed by

electron migration via the external load. In DSSC, there is no permanent chemical change and thus its parts need not be replaced as the components does not undergo any permanent transformation [Gratzel, 2001]. Thus, DSSC is a self-regenerating photo-electrochemical cell (see Figure 2.3b).

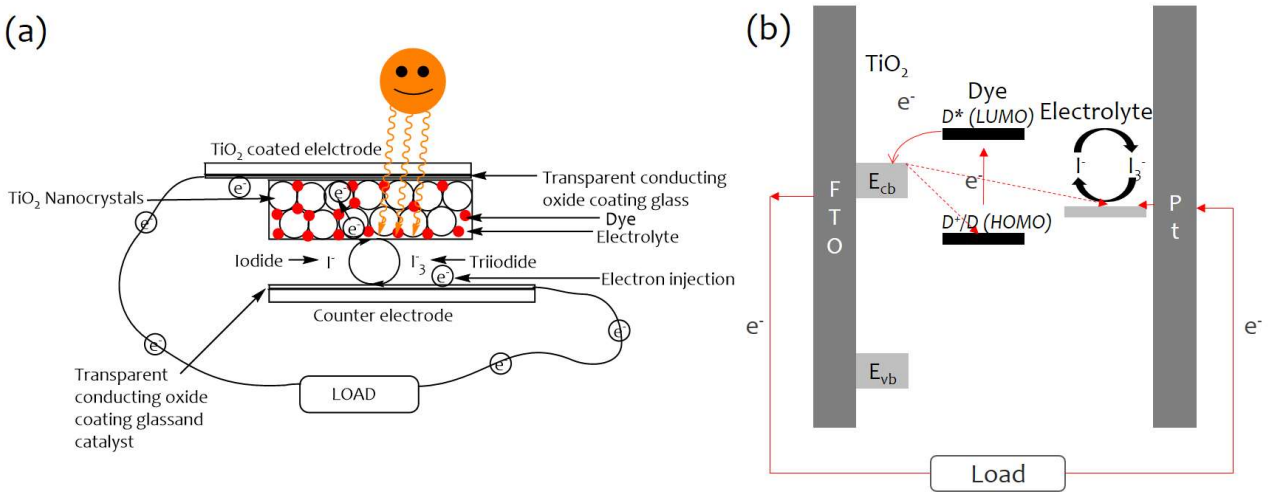

Figure 2.3 : Schematic illustration of (a) DSSC and (b) charge transport in the cell.

Mesoporous TiO_2 at nano range with high crystallinity deposited on the transparent conducting oxide provides large surface area to adsorb dye molecules. When photons fall upon the sensitizer it gets excited from its HOMO to the LUMO represented by Eq. (2.1) and (2.2) The overall process happening can be summed up by the equations as follows:

$$S_{(adsorbed)} + h\nu \rightarrow S^*_{(adsorbed)} \quad (2.1)$$

$$S^*_{(adsorbed)} \rightarrow S^+_{(adsorbed)} + e^-_{(injected)} \quad (2.2)$$

$$I_3^- + 2\,e^-_{(cathode)} \rightarrow 3I^-_{(cathode)} \quad (2.3)$$

$$S^+_{(adsorbed)} + 3/2\,I^- \rightarrow S^*_{(adsorbed)} + 1/2\,I_3^- \quad (2.4)$$

After the electron is injected from the excited state of the dye to the conduction band of the wide band gap mesoporous nanocrystalline semiconductor, the dye is oxidized. Then the injected electron is traveled through the network of TiO_2 interconnects and extracted via the external load where the work done is delivered as an electrical energy. The triiodide-iodide electrolyte system acts as redox electron medium between the TiO_2 photoanode and the Pt counter electrode (Eq. 2.3). This acts as a regenerating system for the oxidized dye molecules by means of receiving electron from the I^- redox mediator that get oxidized to I_3^- (Eq. 2.4) [Nazeeruddin, *et al.*, 2011].

2.2.2 Electron generation, transportation, and recombination

The nanocrystalline TiO_2 used is an interconnect of the colloidal particles with particle size ranging from 15-30 nm and an average thickness of 15 µm [Benkstein, *et al.*, 2003]. A treatment – pre-or post or both is done by the application of $TiCl_4$ for better performance which induces a hazy layer that serves as scattering centers. The usual method of application of TiO_2 over the TCO are done by processes like screen printing, doctor blading and spin coating etc. [Basu, *et al.*, 2016].

Theoretical observations about electron mobility in DSSC assumes the existence of sub band gap states – its location and distribution, in TiO_2 that greatly influence electron transport by means of trapping electron in this system. This observation is inconsistent with the multiple trapping models for charge transport [Byranvand, *et al.*, 2012]. The transport of charges through the interfaces are complex and not ideal and hence the kinetics of the charge transfer taking place in the system depends on a number of factors making it complicated unlike other

processes followed by a rate law. Thus, most of the reaction rates are reported in half times of reaction rate. Some of the processes that are classic method for defining the charge transport processes occurring in DSSC are – electrochemical impedance spectroscopy, open circuit voltage decay, incident photon to current conversion efficiency etc. Fast electron collection is highly significant for efficient working of the redox shuttle that will prevent the loss of photocurrent and also reduces losses from recombination process [Hagfeldt, *et al.*, 2010].

The change kinetics involved in the functioning of a DSSC device can be summarized as:

1) Electron injection and excited state decay

This process is marked by the ultrafast injection of electron from the sensitizer (usually a ruthenium based dye complex) to the conduction band of the wide band gap semiconductor. This is realized within a femtosecond by the dye molecules attached to the TiO_2 surface [Benkö, *et al.*, 2002]. The injection time should be incomparable to the decay of the excited state to the ground state lifetime of the dye molecule. The reported excited lifetime of a Ru based dye is 20-60 ns [Hagfeldt and Grätzel, 2000]. If the electron injection time for the dye is slower, then there might be a crease in the overall performance of the DSSC device.

2) Regeneration of Oxidized dye molecules

The oxidized dye molecules after the excitation are then intercepted by I- within a time domain of microseconds. The expected lifetime of a best performing Ru complex should be >100 s [Wang, *et al.*, 2005]. For a DSSC device to work on outdoor conditions for a long period of time the life cycle of the sensitizer should be greater than 108.

3) Electron transport in the Mesoporous oxide film

The TiO_2 nanocrystalline after depositing or screen printing on the conducting substrates undergo annealing process whereby all the binders and the organic impurities are removed. During this process the TiO_2 layer becomes a compact network through which efficient charge transport takes place. This mesoporous structure has distinct qualities such as (1) low conductivity of the film (2) the individual particle does not support built in electric field (3) the phase boundaries between the semiconducting oxide and the electrolyte containing forms networks providing rooms for huge contact area. It is through this network that the electrons get transferred to the collecting substrate via a hopping mechanism.

4) Recombination of Electrons

Recombination of the photoexcited electron with the oxidized dye. This is the phenomenon in which there is back electron transfer from the conduction band of the semiconductor oxide to the oxidized dye sensitizer, a process occurring at microsecond to millisecond. The time factor depends on the concentration of electron in the semiconductor and hence the light intensity. The electron lifetime is defined as the time that amounts for the recombination of the photoinjected electrons in the conduction band of TiO_2 to recombine with the acceptor in the electrolyte species [Hagfeldt and Graetzel, 1995]. The most abundantly used redox system is the iodide/ triiodide system as they have longer lifetime (1-20 ns) compared to other.

5) Reduction of Electron Acceptors in the Electrolyte at the Counter Electrode

The counter electrode mostly Pt is used, and that is prepared by means of drop casting H_2PtCl_6 on the conducting substrate. by this method charge transfer resistance lesser than 1 ohm cm^2 is obtained [Papageorgiou, *et al.*, 1997].

A picosecond charge injection is required for achieving good quantum yield and long term stability. This also affects the fast recovery of the sensitizer along with adequate charge separation before recombination takes place.

2.2.3 Recent progress in DSSC

TiO_2 is richly used in DSSC as it has the best well-matched band positioning, mesoporous structure with high surface area that gives good dye loading and great electron affinity. The maximum efficiency obtained using TiO_2 is 13%, highest among all other materials used as photoanode [Mathew, *et al.*, 2014]. Various photoanodes apart from TiO_2 has been tested for DSSC over the years. Using hierarchical ZnO with high electron mobility a maximum efficiency of 7.5% has been able to achieve [Memarian, *et al.*, 2011]. Nb_2O_5 with its favorable

band edge shows good electron injection efficiency and offers high circuit potential [Nowak and Ziolek, 1999]. Using Nb_2O_5 nanorods an efficiency of 6% was obtained [Zhang, *et al.*, 2012]. Other metal oxide based nanomaterials have also been used such as Al_2O_3, SnO_2, V_2O_5, ZrO_2, CeO_2 and Fe_2O_3 as photoanode materials in DSSC [Pfeifer, *et al.*, 2013; Scanlon, *et al.*, 2013; Park, *et al.*, 2000]. Apart from this, doping of these nanomaterials [Shejale, *et al.*, 2016; Laishram, *et al.*, 2016] and synthesizing binary metal oxide [Kunzmann, *et al.*, 2016], use of blocking layers are some of the other techniques that are mostly done with the aim of increasing the photoconversion efficiency of the solar cell (see Table 2.2) [Góes, *et al.*, 2012].

Table 2.2: Different material doping in TiO_2 at varying doping percentage.

Sr. No.	*Dopant (doping %)*	*Band gap (eV)*	*Solar cell parameters*			
			J_{sc}	V_{oc}	η	*FF*
1	Zr (5)	3.27	4.5	0.7		
	Zr (10)	3.34	3.2	0.72		
2	Fe_2O_3 (10)	2.51	16.88	0.77	7.27	56
3	Nb (0.7)	3.16	14.4	0.76	8.0	73
	Nb (2.7)	3.12	17.7	0.74	9.0	69
	Nb (3.5)	3.06	18	0.68	8.2	67
4	Zr (4)	2.7	NA	NA	NA	NA
5	Nb (2)*	NA	20.4	1.036	16.3	77
6	Zr (1)	NA	16.5	0.715	8.1	69
7	Fe (10)	2.8	NA	NA	NA	NA
8	Sr (0.06 M)#	3.08	NA	NA	0.69	NA
9	S (0.22)	2.98	NA	NA	NA	NA
10	Ce (10)	2.69	NA	NA	NA	NA
11	Ce (0.03)	1.678	NA	NA	NA	NA
12	Ce (3.5)	2.70	NA	NA	NA	NA
	Nd (1)	3.10				
	Pr (3)	3.10				
	Sm (2)	3.15				
	Gd (2)	3.10				
	Eu (2)	3.05				
	La (3)	3.15				
13	SiO_2	2.88	NA	NA	NA	NA
14	Ag	2.7	NA	NA	NA	NA
15	V_2O_5	2.78	NA	NA	NA	NA
16	CuO	1.44	NA	NA	NA	NA

*Perovskite solar cell; # Photoelectrochemical cell

The various parameters involved in DSSC has been played around with to optimize the efficiency. For dye sensitizer the main focus has been extending the absorbance spectrum by engineering the ligands [Panda, *et al.*, 2012]. The other developments in this field perovskite sensitizer with its incredible light harvesting ability has caught considerable attention with a record PCE up to 20% efficiency [Butler, *et al.*, 2015]. Attempts have also been made to replace the liquid electrolyte system by a more convenient hole transport material in order to avoid the corrosive and leaky nature of the liquid system [Wu, *et al.*, 2015]. Apart from this material scientist are in a quest to find a material that is cheap with good catalytic property which will replace the expensive Pt counter electrode [Wang and Hu, 2012].

In 2009 the halide perovskite with the structure $CH_3NH_3PbX_3$ was first tried as an inorganic sensitizer and gave 3.1% and 3.8% for X as Br and I respectively [Kojima, *et al.*, 2009]. The perovskite structure having band gap of around 1.5eV has good light harvesting capability has attracted attention for solar harvesting [Park, 2015].

Later on, it was increased to 6.54% by Park et al. in 2012 the efficiency was raised to 9.7% and by 2013 it was 12.3% [Im, *et al.*, 2011]. The same year efficiency reported to 15% after which mixed halide perovskite was in used with efficiency of around 10.9% [Park, 2015]. Organohalides based perovskite based solar cells were able to produce greater than 15% efficiency. The efficiency is expected to increase beyond 20% in near future with its salient features like low cost, high efficiency and ease of manufacturing. And 23% efficiency was reported in 2016 by Chen et al of a perovskite and Si mixed tandem solar cell [Chen, *et al.*, 2016].

2.3 PHOTODEGRADATION FOR WATER TREATMENT

2.3.1 Decontamination of water

As a reason of developing new industries and factories, the industrial waste and untreated effluents are discharged into the river and eventually to the seas and oceans because of which these water bodies are contaminated posing great threats to life that are dependent on water – plants, animals and humans alike. Thus, curtailing the pollution level is one of the major task that we as humans need to do. Thus, waste and polluted water treatment to remove the organic pollutants from the water bodies to a permissible level is of utmost importance.

The level of pollution in water bodies is mainly characterized by two parameters – Chemical Oxygen Demand and Biological Oxygen Demand [Rani and Dahiya, 2008]. Minimizing the values of COD and BOD have been the main focus in many countries to address the environmental problems and health issues. Some of the techniques employed to reduce the COD and BOD value includes biochemically based systems, film reactor, Fenton oxidation, electrochemical treatment and other photolytic process. These conventional methods have its own shortcomings e.g., release of methane gas as a byproduct contributing to global warming, limiting span of the fixed film reactor.

The Fenton oxidation technique requires further treatment of the iron-containing sludge released as a byproduct which contains high concentration of ferrous iron salts [Mills, *et al.*, 1993]. The drawbacks of these techniques are the high operational costs and partial degradation of the pollutants.

With an aim to find a technology that fulfills the downsides of the conventional system, the photodegradation of water treatment is placed – low cost and high efficiency. The use of heterogeneous catalyst for water treatment by means of advanced oxidation technology can be a promising method. By this means, the organic impurities are reduced to various constituents like carbon dioxide, water vapor and inorganic substances with the help of sunlight to convert the polluted water to clean water.

Photodegradation using catalyst is done such that the catalysts absorb photon creating excited and energetic hole and electrons that perform the redox reactions [Guo, *et al.*, 2016]. The discovery of photocatalytic water splitting using TiO_2 by Fujishima and Honda [Fujishima and Honda, 1972] in 1972 led to the opening of a whole new field of water splitting and wastewater degradation.

Some major setbacks holding this technology behind are the low photocatalytic efficiency, narrow band spectrum for solar absorption, particulate nanoparticles used in batches for the degradation process and the high cost of further recovery of the used catalyst from water. Thus, in order to be a good photocatalyst, it should absorb in a wide range of spectrum ranging from the UV-Vis to the near IR region but hardly any material exists that absorbs the desired range of spectrum. Thus, the main aim of researchers today is to develop photocatalyst that delivers high performance with a wide range of absorption for solar light at low costs. The photodegradation kinetically depend on some major factors – amount of catalyst used, wavelength and light irradiation, intensity of the light used and dimensions of the reactor system.

2.3.2 Basic mechanism of photodegradation

The mechanism of the photodegradation using catalyst can be divided into various stages. The first is the light absorption which is mainly dependent on the band gap of the

material E_g of the semiconductor material used. When light falls upon the material, if the energy is greater than E_g then electrons (e^-) are excited from the valence band (VB) to the conduction band (CB) of TiO_2 leaving positively charged holes (h^+) behind. In the next stage, there is a conversion process whereby the electrons and holes - recombine and dissipate the absorbed energy as heat, react with other donors and acceptors or become trapped in metastable surface states (see Figure 2.4) [Hoffmann, *et al.*, 1995].

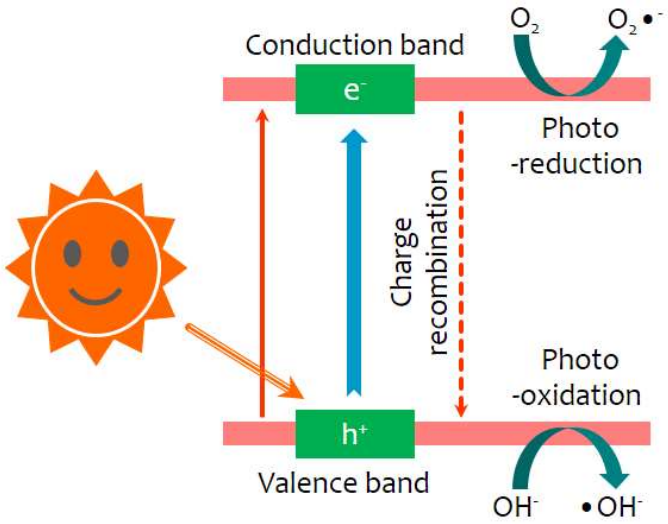

Figure 2.4 : Schematic representing the mechanism of photodegradation under sunlight

The different facets of the crystalline semiconductor have varying surface energy and it determines the amount of photo induced e^- and h^+. The transportation of the charge carriers as it undergoes redox reaction with other species on the surface of the semiconductor. Thus, for effective photodegradation, the photocatalyst is expected to possess the following features: (i) good light absorption over wide range of spectrum (ii) high surface area with its specific sites exposed with large no active surface sites (iii) morphological enhanced to provide better charge separation or inhibit recombination [Tian, *et al.*, 2014].

The charge transfer and recombination rates is a result of different structures and various surface morphologies. Some of the most widely used UV-Vis active photocatalyst for this purpose are TiO_2, ZnO, WO_3, $BiVO_4$/Ag_3VO_4, CdS quantum dots, SnO_2/Zn_2SnO_4, Bi_2WO_6 (see Table 2.3) [McLaren, *et al.*, 2009; Xi, *et al.*, 2012; Yan, *et al.*, 2016; Samadi-Maybodi and Sadeghi-Maleki, 2016; Dong, *et al.*, 2015; Tian, *et al.*, 2013].

Table 2.3 : Comparison of various photocatalyst with their optical and surface properties and their pollution degradation efficiency

Photocatalyst	*Optical properties and bandgap*	*BET surface area ($m^2 g^{-1}$)*	*Pollutant*	*Degradation efficiency or reaction rate*
WO_3–TiO_2/AC	-	498	10 mg L^{-1} congo red	81.46%
C-doped Bi_2O_3	Visible light absorption band at 450–530 nm, absorption edge of C-doped Bi_2O_3 has red-shift	5.9	13 mg L^{-1} methyl orange	95%
TiO_2	Moderately absorbed at 385 nm and strongly around 300-350 nm	261.7	Acetaldehyde	0.0005 min^{-1}

C–N–TiO_2 (N(o))	Absorption edge shift to visible range	59	5 mg L^{-1} RhB	48%, 0.0049 min^{-1}
N-TiO_2	Absorption threshold at 406 nm	78.5	20 mg L^{-1} phenol	41.9%
ZnO	Absorption edge from 400 nm to 800 nm	57.3	3 mg L^{-1} MB	85%, 0.0337 min^{-1}
C_{60}-ZnO	Absorption intensity increases with C_{60} amount	56.9	3 mg L^{-1} MB	95%, 0.0569 min^{-1}
A-$BiVO_4$	Absorption edge blue shifts as pH values increase, 560 nm (4.9 pH)	10.3	5 mg L^{-1} RhB	61%

Organic dyes that are released mainly from the dying industries and from other sources like textile, printing and photographic industry as well. These are released as effluents into the water stream which affects badly even at low concentrations as it is hard to biodegrade or oxidized even with the aid of chemicals. It is possible to degrade in aqueous solution under the effect of visible light [He, *et al.*, 2014].

High surface area and crystallinity are important factors that govern the reaction efficiency. For example, Bismuth titanate ($Bi_{12}TiO_{20}$) showed better removal of acid orange 7 under visible light than in comparison to N-doped TiO_2 [Zhu, *et al.*, 2010]. Apart from this, lowering defects and photosensitization capability affects the photodegradation activity. It was observed that microscale ZnO showed higher photocatalytic activity than TiO_2 under visible light as the photosensitization efficiency of transferring electron from the excited dye molecule to the conduction band of the semiconductor oxide is higher for the former. Moreover, microscale sized ZnO exhibited better photostability than nanoscale ZnO. Thus, a modified structure of TiO_2 and ZnO was developed to garner more photon conversion efficiency thereby increasing the photocatalytic dye removal from wastewater [Li, *et al.*, 2010]. Pharmaceutical and personal care products are also emerging contaminants polluting water. Some of the drugs like oxytetracycline have been studied for photochemical degradation [Zhao, *et al.*, 2013]. Phenol containing compounds are reportedly difficult to biodegrade because of the presence of stable benzene rings and cause diseases like cancer, angiocardiopathy and gastroenterology etc., even at very low concentrations. These compounds are commonly and widely present in water waste from petroleum, coal and chemical industries. However, by means of visible light responsive catalyst, most phenol containing compounds have been degraded effectively. Using layered perovskite La_2NiO_4 photocatalyst, 4-chlorophenol was mineralized under visible light [Yiming He, *et al.*, 2014].

Residual ions and acids like hexavalent chromium (Cr(VI)) that are present as inorganic impurities in wastewater as carcinogenic and mutagenic pollutants. These inorganic pollutants go into water via pigment production, metal plating and leather tanning, etc. Thus Cr(VI) visible light driven reduction at low cost with good efficiency has received attention in recent years [Wang, *et al.*, 2013; Yang, *et al.*, 2013]. For example, flower-like nanostructures $SnIn_4S_8$ with strong visible absorption, high surface area and good charge separation were used for efficient reduction of aqueous Cr(VI) and showed excellent degradation and good photostability. In this case, the photoexcited exciton pairs migrate to the surface of the nanoparticle to participate in redox reaction from where the e^- and the h^+ reduces the absorbed Cr(VI) to Cr(III) and oxidize water to oxygen respectively.

2.4 CLOSED SHELL METAL OXIDES

Metal oxides exhibit varying degree of behavior in its chemical, electrical, optical and magnetic properties. Closed shell metal oxides are a class of solid formed by combination of oxide ions of metal ions with filled electronic shell with oxides of series of metals from

transition-, lanthanum-, and actinium series with incomplete electronic shell. Other insulating compounds are known to have electronic configurations with close shell diamagnetic ground state. For example, CuO, Ag_2O_3, PdO, $LaCoO_3$, $LaRhO_3$. The band gap of these compounds are essential because of the crystal field splitting of d levels. For the perovskite compounds the closed shell state is achieved by filling up of low spin d^6 compounds, the band gap in this case is due to filling of t_{2g} band and empty E_g band. The d^{10} configuration found in these compounds have band gap with filled nd levels and empty (n+1)s as in case of CuO with filled 3d and empty 4s. Other post-transition materials like Zn and Sn have d^{10} configuration as in ZnO and SnO_2 where the valence band is formed by oxygen 2p orbitals along with d^0 oxides. Thus, the level of energy gap of the uppermost filled O 2p and the lowest empty band depends on the electronic configuration of the particular metal forming that oxide. Also, E_g is directly proportional to the electronegativity difference of the metal forming the compound. Apart from this, E_g also varies with the value of principal quantum value n of the metal atoms [Cox, 2010].

Closed shell metal oxides are thus classified as insulators like MgO and Al_2O_3 and semiconductors like ZnO, PbO etc. [Law, *et al.*, 2005]. These metal oxides e.g, ZnO and TiO_2 are used as photoanode in DSSC to increase the efficiency [Varghese, *et al.*, 2009]. Efforts are being made to develop materials that have properties to harness more photons and better charge separation to increase the charge collection efficiency without distressing other parameters involved [Dang, *et al.*, 2011]. Metal oxide core shell like Ag with TiO_2 nanostructured localized surface plasmon with potential for improving light absorption and in turn performance of the device have been reported [Qi, *et al.*, 2011]. The mechanism behind this works is by a metal nanoparticle acts as a covering to prevent back reaction or recombination and also from corroding by the electrolyte. This arrangement of core shell metal oxide nanoparticles demonstrated improved efficiency up to 9% while the thickness was decreased by 25% thus improving the electron collection. Also, the material usage has also been reduced by 62% at the cost of the same efficiency[Lu, *et al.*, 2010]. Apart from these LSP, hollow sphere metal oxides with size ranging from micrometer to nanometer range with controlled internal structure and shell composition have found usage in old age heterogeneous catalysis and upcoming technologies like drug delivery with prolonged release time, energy conversion systems, sensors, biotechnology, photocatalysis and photonic devices, etc. [Wang, *et al.*, 2009; Walsh and Mann, 1995; Benabid, *et al.*, 2005; An and Hyeon, 2009; Yang, *et al.*, 2008; Wei, *et al.*, 2008; Yang and Zeng, 2004; Liu, *et al.*, 2010]. Various methods have been reported for synthesizing single and doubled shelled nanoparticles such as vesicles, emulsions, micelles, gas bubble and hard templating methods, etc. [Schacht, *et al.*, 1996; Lou, *et al.*, 2008; Huang, *et al.*, 2000; Caruso, *et al.*, 1998]. The Cu_2O [Xu and Wang, 2007], multiple-shell azithromycin [Zhao, *et al.*, 2008], SnO_2 [Yang, *et al.*, 2007] and multiple-shell Co_3O_4 [Wang, *et al.*, 2010] hollow microspheres with enhanced properties were fabricated by various synthesis methods suited to each specific materials. Carbonaceous microspheres saturated with desired metal when heated in air is left with the formation of metal oxide shells and the shell layers depend on the loading of the metal [Lai, *et al.*, 2011]. Apart from this, thermal activation using closed shell gas phase gold doped TiO_2 clusters, $AuTi_3O_7$ was performed which showed that closed shell metal oxide is reactive enough to facilitate certain bond cleavages [Nagata, *et al.*, 2016]. Similar thermal activation for methane has been performed by Al/Ta heteronuclear clusters whereby efficient chemisorption of methane takes place by the closed-shell oxide $[Al_2TaO_5]^+$ at ambient conditions with the formation of $[Al_2TaO_4(OH)(CH_3)]^+$ [Zhou, *et al.*, 2016]. Also, thermal activation of methane by $[HfO]C^+$ and $[XHfO]^+$ (X = F, Cl, Br, I) has been reported by Zhou et al [Zhou, *et al.*, 2016].

Mostly, in close shell metal oxide, temperature variation is a key parameter studied for controlling various physical and chemical properties of TiO_2 nanostructure [Cozzoli, *et al.*, 2003]. Among the serval techniques, sol-gel is one of the most studied method to prepare anatase, rutile and brookite nano-titania at low temperature [Cantau, *et al.*, 2010; Mutuma, *et al.*, 2015]. The lowest temperature ever reported for preparation of TiO_2 is 4°C [Burunkaya, *et al.*, 2013] and further studies on synthesis of titania below 0°C temperatures are virtually absent in the literature, Table 2.4 summarized the literature brief about the synthesis of titania at low temperature.

Table 2.4 : Literature brief about synthesis of titania at low temperature

Sr. No.	*Article*	*Synthesis Method*	*Precursor for TiO_2 Synthesis*	*Low Synthesis Temp. (°C)*	*Phase*
1.	[Leyva-Porras, *et al.*, 2015]	Sol-gel	TTIP	25 to 80	A
2.	[Jin, *et al.*, 2015]	Wet Condition	TTIP and TiO_2 Nanowire bundles	40	A & R
3.	[Li, *et al.*, 2015]	Hydrolysis	Tetrabutyl titanate	RT	A
4.	[Elgh and Palmqvist, 2015]	Hydrolysis	Titanium n-butoxide	40 to 70	A, R & B
5.	[Graciani, *et al.*, 2015]	Sputtering	TiO_2 crystal	RT	R
6.	[Zhang, 2015]	Hydrothermal	$Ti(SO_4)_2$	90	A
7.	[Safeen, *et al.*, 2015]	Sputtering	Ceramic TiO_2 disc	RT to 400	A & R
8.	[Ishii, *et al.*, 2015]	PLD	TiO_2 pellet	RT to 600	R
9.	[Bu, *et al.*, 2015]	Hydrolysis	Tetra-n-butyl titanate	70	A
10.	[Li, *et al.*, 2014]	Hydrothermal	Tetrabutyl titanate	180	A
11.	[Mutuma, *et al.*, 2015]	Sol-gel	TTIP	RT	A, R & B
12.	[Yan, *et al.*, 2005]	Hydrothermal	Tetrabutyl titanate	RT	A& R
13.	[Wang, *et al.*, 2007]	Hydrolysis	$TiCl_4$	50	R
14.	[Cozzoli, *et al.*, 2003]	Hydrolysis	TTIP	80	A
15.	[Cui, *et al.*, 2015]	Sol-gel	TTIP	50	A
16.	[Jouenne, *et al.*, 2015]	Hydrolysis	$[Ti_8O_{12}(H_2O)_{24}]Cl_8{\cdot}HCl{\cdot}_7 H_2O$	RT	A & R
17.	[Luo, *et al.*, 2015]	Sol-gel	Tetrabutyl titanate	50 to 90	A
18.	[Sheikhnejad-Bishe, *et al.*, 2014]	Sol-gel	Tetrabutyl titanate	50	A & B
19.	[Pookmanee, *et al.*, 2013]	Hydrothermal	TTIP	100 to 200	A
20.	[Dai, *et al.*, 2014]	Hydrothermal	Tetrabutyl titanate	100	A & B
21.	[Mishra, *et al.*, 2013]	Sol-gel	$TiCl_4$	15 to 35	A
22.	[Mamakhel, *et al.*, 2013]	Hydrothermal	TTIP	RT to 200	R
23.	[Li, *et al.*, 2013]	Sol-gel	TTIP	40 to 75	A & R
24.	[Lo, *et al.*, 2013]	Hydrothermal	TTIP	70	R
25.	[Rashad, *et al.*, 2013]	Hydrothermal	TTIP	100	A & R
26.	[Brahmi, *et al.*, 2013]	Sol-gel	TTIP	60	A
27.	[Jing, *et al.*, 2013]	Sol-gel	Titanium n-butoxide	80	A
28.	[Valencia, *et al.*, 2013]	Sol-gel	TTIP	200	A
29.	[Sasani Ghamsari, *et al.*, 2013]	Sol-gel	TTIP	100	A
30.	[Burunkaya, *et al.*, 2013]	Sol-gel	Titanium ethoxide	4	A
31.	[Lai, *et al.*, 2012]	Hydrothermal	$TiCl_4$	120	A
32.	[Kovash, *et al.*, 2012]	Hydrolysis	TTIP	80	-

33.	[Jiang, *et al.*, 2011]	Hydrolysis	Tetrabutyl titanate	15	A & B
34.	[Cantau, *et al.*, 2010]	Sol-gel	TTIP	RT	A & R
35.	[Nikkanen, *et al.*, 2007]	Sol-gel	Titanium butoxide	50	A & R
36.	[Sayılkan, *et al.*, 2006]	Hydrothermal	TTIP	200	A
37.	[Maver, *et al.*, 2009]	Sol-gel	TTIP	85	A
38.	[Li, *et al.*, 2009]	Hydrolysis	Tetrabutyl titanate	40 to 120	A
39.	[Chuang and Chen, 2008]	Sol-gel	Tetra-n-butyl titanate	103	A
40.	[Zhai, *et al.*, 2008]	Sol-gel	$TiCl_4$	40	R
41.	[Chen and Shen, 2008]	Hydrolysis	Titanyl diacetate & titanyl dibutoxide tetraacetate	60 to 80	A
42.	[Xu, *et al.*, 2008]	Sol-gel	Tetrabutyl titanate	75	A
43.	[Wang, *et al.*, 2008]	Sol-gel	Titanium(IV) Sulfate	70	R
44.	[Qi, *et al.*, 2010]	Hydrolysis	$TiCl_4$	100	R
45.	[Zhou, *et al.*, 2010]	Hydrothermal	Titanium(IV) Sulfate	160	A
46.	[Laskova, *et al.*, 2015]	Hydrolysis	Titanium(IV) butoxide	200	100% A
47.	[Ahmad, *et al.*, 2016]	Hydrothermal	Titanium(IV) butoxide	150	100% R